Deformation of post-spinel under the lower mantle conditions

F. Xu[1, 2], D. Yamazaki[1], S. A. Hunt[3, 2], N. Tsujino[1], Y. Higo[4], Y. Tange[4], K. Ohara[4], D. P. Dobson[2]

[1] Institute for Planetary Materials, Okayama University, Misasa, 682-0193 Tottori, Japan
[2] Department of Earth Sciences, University College London, Gower Street, London WC1E 6BT, United Kingdom
[3] Department of Materials, University of Manchester, Sackville Street Building, Manchester M1 3BB, United Kingdom
[4] Japan Synchrotron Radiation Research Institute, SPring-8, Sayo, Hyogo 679-5198, Japan

Key Points

- Deformation experiments were conducted on pre-synthesized post-spinel and bridgmanite two-layered samples using DT-Cup apparatus
- No weakening was observed up to the strain of 0.25, bridgmanite dominates the bulk rheology under the current experimental conditions

Abstract

To study the viscosity of bridgmanite and ferropericlase aggregate, uniaxial compression deformation experiments on pre-synthesized post-spinel phase and bridgmanite two-layered samples were conducted under top lower mantle pressure and 1773 K utilizing DT-Cup apparatus. Up to the strain of 0.25±0.05, the observed comparable strain of the bridgmanite and post-spinel samples suggests the bridgmanite dominates the bulk viscosity of the post-spinel without strain localization in periclase. The microstructures of the deformed post-spinel samples show evidence of similar strain of periclase with the bulk strain without strain partitioning. Texture analyses of bridgmanite indicate a dominant slip plane (100), with a steady state fabric strength achieved within strain of 0.12±0.01. The current experiment has provided no evidence about an onset of strain localization of ~30 vol.% periclase at 0.25 strain. Our observations provide direct experimental verification of bridgmanite controlled rheology under low strain magnitude, which should be considered in geodynamical models which include mantle compositional and rheological evolution in the lower mantle.

Plain language Summary

The Earth’s lower mantle occupies ~65% volume of Earth’s mantle and plays an important role in mantle dynamics. The major constituent mineral of the lower mantle, bridgmanite, might dominate the rheology of the lower mantle. On the other hand, despite its small proportion, there is a chance that ferropericlase controls the rheology of the lower mantle due to its significant softness compared with bridgmanite. In this study, we conducted uniaxial deformation experiments on pre-synthesized post-spinel (∼70% bridgmanite +∼30% periclase) and bridgmanite two-layered samples under top-most lower mantle conditions up to strain of 0.25±0.05. The bridgmanite and post-spinel samples showed similar strains, suggesting that the bridgmanite controls the bulk strength of the post-spinel. This result is significant for understanding the viscosity structure of Earth's lower mantle.

1. Introduction

The lower mantle is thought to be composed primarily of the minerals bridgmanite (perovskite-structured $(Mg,Fe)SiO_3$) and ferropericlase ($(Mg,Fe)O$) with minor amounts of a calcium-silicate perovskite phase. It has been suggested that the Mg/Si ratio in the lower mantle may vary, resulting in varying bridgmanite-ferropericlase concentrations. Pyrolitic composition model with Mg/Si atomic ratio of ∼1.3 hosts ∼77% bridgmanite and up to ∼16% ferropericlase in the lower mantle, in addition to ~8% of calcium-perovskite (e.g., Irifune, 1994; Irifune et al., 2010). In contrast, a primordial near-chondritic composition with Mg/Si ratio of ∼1.0 results in a bridgmanite-dominated lower mantle (> 93%) with a minor amount of ferropericlase and calcium-silicate perovskite (Murakami et al., 2012). Furthermore, there is increasing geophysical evidence for compositional heterogeneity in the lower mantle, and this might have implications for its rheology and dynamic evolution. One mechanism for generating compositional heterogeneity in the lower mantle is the recycling of subducted oceanic lithosphere which is differentiated into a depleted, harzburgitic (Mg-rich) component and an enriched basaltic (Si-rich) component (Irifune & Ringwood, 1987). A compositionally layered lower mantle related to re-fertilization by subducting basaltic component has been proposed to have a low Mg/Si lower mantle (Ballmer et al., 2015).

A compositionally heterogeneous lower mantle may exhibit heterogeneous deformation, which depends on the rheological contrast between the different phases and their morphology within the rock. Ferropericlase is likely much weaker than bridgmanite under lower mantle conditions (Yamazaki & Karato, 2001), so it may significantly affect the rheology of the composite of ferropericlase and bridgmanite, depending on the stress and strain partitioning between it and the volumetrically dominant bridgmanite component (Handy, 1994).

Slab stagnation is widely observed in the mid-mantle at ~1000 km depth (e.g., Fukao & Obayashi, 2013; Li et al., 2008), corresponding to the depth where inversions of geophysical observables prefer a maximum in viscosity (e.g., Rudolph et al., 2015). This barrier to subduction may originate from bridgmanite-enriched ancient mantle structures (BEAMS), low Mg/Si ratio regimes separated by channels of pyrolitic material with higher Mg/Si rocks (Ballmer et al., 2017). The BEAMS could be a good candidate to host primordial geochemical signatures in Earth's interior that should have been isolated since Earth's formation (Mundl et al., 2017). However, the formation and preservation of BEAMS are highly dependent on its viscosity contrast with pyrolytic composition, i.e., a 20-fold difference is required to prevent efficient mixing (Ballmer et al., 2017).

Although many studies have been focused on this issue, the role of ferropericlase in the rheology of the lower mantle is still controversial. Finite element modeling (FEM) of deformation in bridgmanite-ferropericlase aggregates by Madi et al. (2005) found bridgmanite controls deformation even when both phases are highly interconnected. Wang et al. (2013) deformed 72% $CaGeO_3$-perovskite with 28% isolated MgO aggregate in the D-DIA up to 20% axial shortening and found that the bridgmanite analogue ($CaGeO_3$) controlled deformation. However, by the deformation of a mixture of $NaMgF_3$ with various concentrations of NaCl (Kaercher et al., 2016), the chloride (ferropericlase analogue) was found to control the deformation even at concentrations as low as 15 vol.%. This may be due to the microstructure of their starting aggregates, in which the NaCl grains were interconnected. Recently, using rotational Drickamer apparatus, Girard et al. (2016) presented the first successful post-spinel (~70% bridgmanite +~30% ferropericlase) deformation experiments under lower mantle conditions, up to 100% shear strain. They suggested that, even though it was not interconnected in recovered samples, ferropericlase controlled deformation based on observations of strain weakening during deformation and microstructure of two phases after recovering. To date, the relationship between microstructure (whether the weak phase was interconnected) and which phase controls the viscosity is still controversial (Table S1).

The bulk viscosity of the aggregates depends strongly on the viscosity contrast, the microstructure and the mechanisms by which deformation occurs of the constituent two phases (Handy, 1994). Moreover, they are highly dependent on pressure, temperature and evolve with strain, which renders it difficult to extrapolate by analogy from low pressures. Therefore, experiments on bridgmanite and ferropericlase under lower mantle conditions are essential. *In situ* deformation experiments by Girard et al. (2016) lack the information of structure evolution with increasing strain, which is particularly important for understanding the microstructure effect on the bulk viscosity. In this study, we firstly synthesized statically annealed bridgmanite ($MgSiO_3$ composition) and periclase (MgO composition) aggregate with isolated periclase grains inside of a bridgmanite matrix. Uniaxial deformation experiments were then performed using DT-Cup apparatus (Hunt et al., 2014, 2019; Hunt & Dobson, 2017). To understand the viscosity of bridgmanite and periclase mixture, the relative viscosity of two-layered samples composed of post-spinel aggregate and pure bridgmanite aggregate is obtained.

2. Experiment

2.1 Synthesis of starting materials

We pre-synthesized polycrystalline aggregates of post-spinel and bridgmanite as starting materials of deformation experiments at high pressure and high temperature in the Kawai-type multi-anvil apparatus installed at Institute for Planetary Materials, Okayama University, Japan. To avoid the possible effect of grain size on the strength and development of lattice preferred orientation, post-spinel and bridgmanite samples with similar grain sizes of 5-10 μm were synthesized.

For the synthesis of post-spinel, forsterite (Mg_2SiO_4) gel was used as starting material. The starting material was wrapped with a platinum capsule and compressed to ~25 GPa and annealed at 2073 K for 3 h. Polycrystalline samples of bridgmanite were synthesized from $MgSiO_3$ bulk glass. The glasses were quenched from a molten oxide mixture of MgO + SiO_2 (1:1 by mole ratio) with a conical nozzle levitation (CNL) method at BL04B2, SPring-8, Japan (Ohara et al., 2020). The recovered glass ball was core-drilled with a diameter of 0.7 mm by an ultrasonic coring machine for synthesis. The glass rod was encapsulated by platinum and compressed to ~27 GPa with ~3 GPa overpressure (i.e., the pressure above the equilibrium phase boundary between akimotoite and bridgmanite) and fast heated to 1873 K (from 673 to 1573 K in 18 s) to enhance nucleation process (Nishiyama et al., 2012). The sample was quenched by shutting down the power supply after annealing for 5 mins.

After synthesis experiments, the recovered sample was mounted in epoxy resin and polished by sandpaper, diamond paste and colloidal silica in sequence. Micro-focused X-ray diffractometer (RINT RAPID II, RIGAKU Co., Japan) with 100 μm X-ray beam from a rotating Cu anode (λ Kα1 = 1.54060 Å) was used for phase identification. The observation of microstructure was done using a field emission scanning electron microscope (SEM) (JSM-7001F, JEOL Co., Japan) installed at Institute for Planetary Materials, Okayama University, with an accelerating voltage of 15 kV and a beam current of 5 nA. Ultimately, well-sintered samples were shaped to cylinders with a diameter of ~0.7 mm by ultrasonic coring machine and sliced with a thickness of 0.3 mm for deformation experiments.

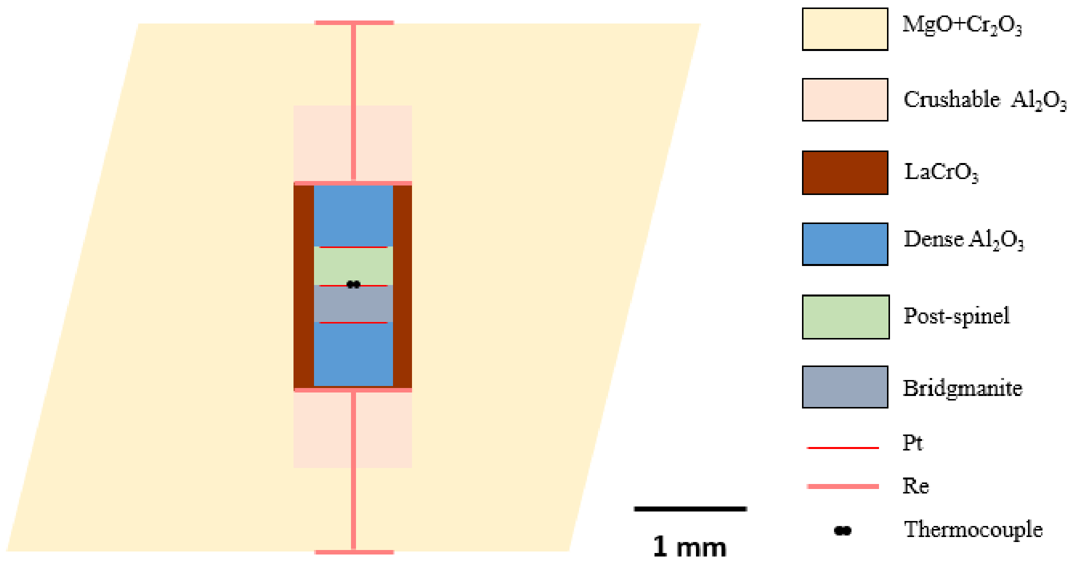

Fig. 1 Configuration of cell assembly for uniaxial deformation experiment in DT-Cup apparatus.

2.2 Deformation experiment

Deformation experiments were conducted using a DT-Cup apparatus (Hunt et al., 2014; Hunt & Dobson, 2017) installed at University College London, UK (Table 1). The pressure was generated by 1.5 mm truncated WC anvils combined with 5.74 mm $MgO+5\%Cr_2O_3$ pressure media (Fig. 1). High temperature was realized by a $LaCrO_3$ heater and monitored by the thermocouple which was sandwiched by samples at the center of heater. Two-layered samples of post-spinel and bridgmanite aggregate were stacked along the compression column together for deformation. As the same stress and chemical condition of deformation (e.g., oxygen fugacity, water fugacity), we can have a direct comparison of the relative strengths of the sample by the strain contrast (e.g., Hunt et al., 2019; Li et al., 2007). To avoid the deformation of sample during cold compression, crushable Al_2O_3 pistons were set at the two ends of the sample column. Hard Al_2O_3 pistons were set near the sample to induce stress during deformation. Two 25 μm thickness Re foils were inserted in the $MgO+5\%Cr_2O_3$ and crushable Al_2O_3 piston to be the electrode. 10 μm thickness Pt foils were placed at the ends of samples as the strain marker.

The sample was first compressed to the target load at room temperature with the differential actuator fully retracted, and the temperature was increased to 1773 K. Ahead of deformation, the temperature was kept at 1773 K for about 1 h for annealing. Before deformation, the differential oil pumps were advanced rapidly, usually with a speed of 10 ml/min, until the differential pistons were lifted from their retracted positions, which was indicated by the displacement transducer of the differential rams. The sample was subsequentially deformed with advancing upper and lower anvils with a constant oil pump rate (0.25 ml/min for 2 h in these experiments). After deformation finished, the experiment was quenched and decompressed whilst maintaining the position of differential rams.

2.3 Sample analysis for recovered samples

After experiments, the recovered samples were detached from other parts of cell assembly, mounted in epoxy resin and polished parallel to the cylindrical axis using sandpapers and diamond paste. The microstructure of recovered samples was observed by SEM (as described above). The double end polished sample before the experiment was measured by digital-caliper to obtain length. The sample length after deformation was measured in the image of SEM which was marked by the Pt strain marker. The strain was estimated from the change of sample lengths before and after deformation experiments. The uneven shape of the strain marker section is the main error source for the strain calculation. We simply calculated the averaged strain rate with total strain and duration of the deformation under the assumption of a constant rate of length change during deformation.

Backscattered electron (BSE) images of post-spinel samples were acquired for microstructures analysis to characterize morphology of periclase grains. First, periclase grains were separated from bridgmanite by a threshold method of image processing with Image J. Then, the grain size and long axis of grain were obtained by elliptical approximation of each periclase grain. The analyzed area covered whole polished surface of the post-spinel sample. For discussing the effect of periclase interconnectivity on rheology of the aggregate, the size of interconnected clusters of periclase grains is the important property (e.g. Heilbronner, 1992; Thielmann et al., 2020). The distribution in cluster sizes is given by the cluster correlation function C_2^i, where i denotes the function pertains to the ith phase (in the present case, only periclase is important so we dispense with the superscript). The cluster function is derived by calculating the correlation function of each individual cluster with itself but with no other clusters. Bitmap images of individual periclase clusters were extracted from the binary images and their autocorrelation functions were averaged to generate the C_2 function for each image.

As bridgmanite is highly sensitive to electron beam radiation, electron backscatter diffraction (EBSD) cannot be utilized to obtain the lattice preferred orientation (LPO) pattern. Thus, the LPO of bridgmanite was determined using the two-dimensional (2D) monochromatic X-ray diffraction pattern detected with image plate (IP) at BL04B1, SPring-8, Japan. The diffraction was collected with a beam energy of 61.5 keV and size of 200 μm×100 μm to 400 μm×400 μm for 15 min. Fig. S1a represents the one-dimensional data converted from 2D data. LPO is exhibited as regular intensity variations in Debye rings along the azimuth angle (Fig. S1b, c). The LPO was calculated using the software package of ReciPro (Seto et al., 2010; Seto, 2012) by simulating the obtained 2D data (as used previously by, e.g., Tsujino et al., 2016). Distributions of misorientation angles are calculated from the randomly selected simulated grains. To quantitatively evaluate the fabric strength, *M*-index, which gives the difference of misorientation angles distribution between the deformed bridgmanite and a theoretical random fabric, was calculated based on the simulated LPO result (Skemer et al., 2005). The samples were measured with the uniaxial compressional direction both perpendicular (along ψ=0 and 90°) and parallel to the direction of the X-ray beam to check the reproducibility of the method.

The LPO of periclase was evaluated by the indexation of the EBSD patterns using the SEM-based EBSD installed at Institute for Planetary Materials, Okayama University, Japan. The EBSD pattern of each periclase grain was obtained at 15 kV acceleration voltage and 5.0 nA probe current. The EBSD patterns were indexed with HKL CHANNEL5 software (Oxford Instruments, Ltd.). The measurement was performed on a grain-by-grain basis over the post-spinel sample and in opertor-controlled indexing mode to obtain an accurate solution. The crystallographic orientation of 240-300 grains of periclase was measured for each sample.

3. Results

3.1 Microstructure

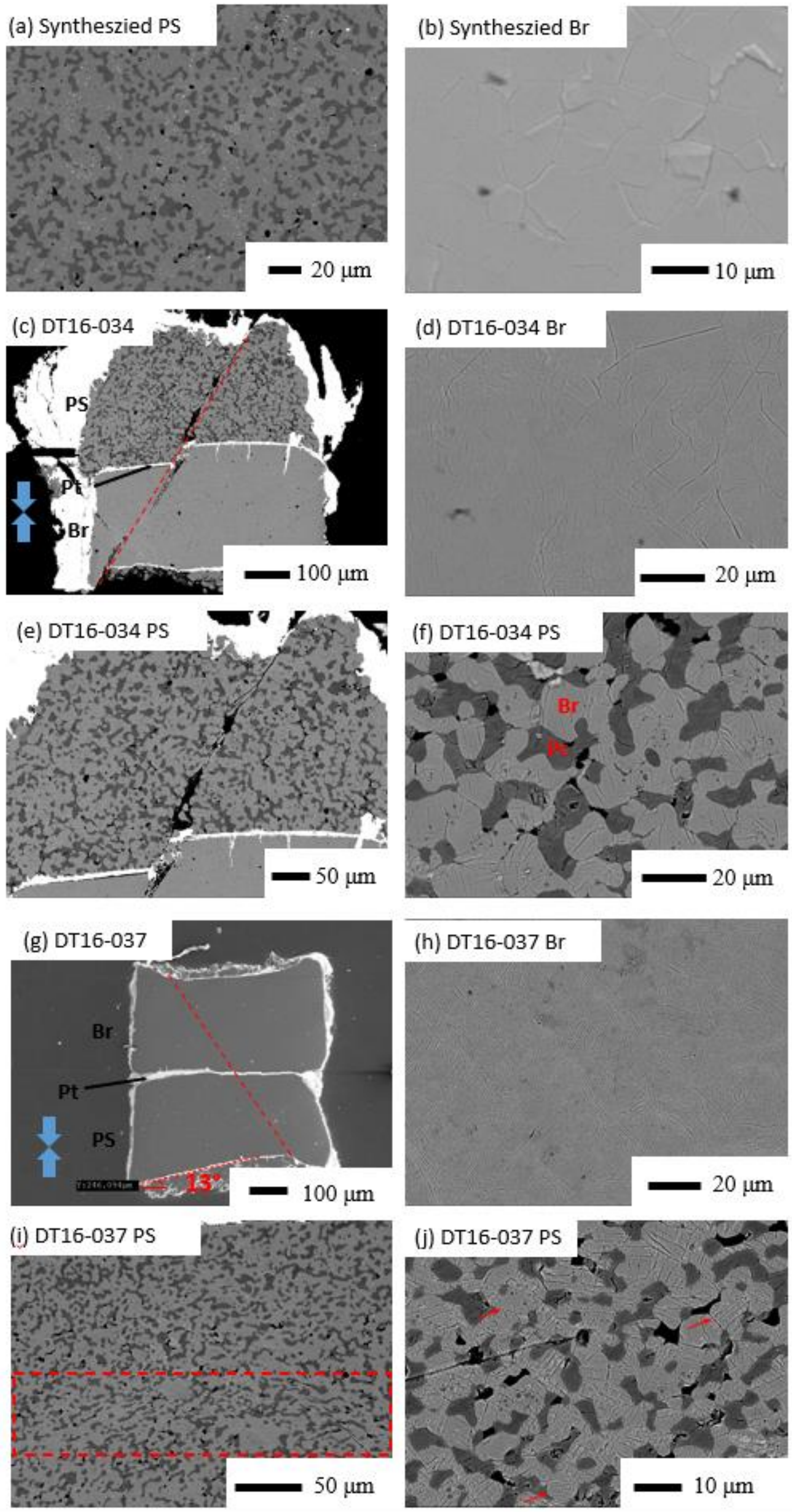
(a) Syntheszied PS
20 μm
(b) Syntheszied Br
10 μm
(c) DT16-034
PS
Pt
Br
100 μm
(d) DT16-034 Br
20 μm
(e) DT16-034 PS
50 μm
(f) DT16-034 PS
Br
Pc
20 μm
(g) DT16-037
Br
Pt
PS
13°
100 μm
(h) DT16-037 Br
20 μm
(i) DT16-037 PS
50 μm
(j) DT16-037 PS
10 μm

Fig. 2 Representative images of undeformed post-spinel (PS) and bridgmanite (Br) samples (after synthesis) (a, b) and recovered samples after deformation (c-f, DT16-034; g-j, DT16-037). All images are backscattered images except for (g), in which a secondary electron image is shown. The dark and light grains in PS composite (a, c, e, f, i and j) are periclase (Pc) and Br, respectively, as marked in (f). The blue arrows in (c) and (g) represent the direction of uniaxial compression. The dashed lines (c) and (g) marked the position of crack formed in the sample after and prior to deformation, respectively. The red dashed line in (g) indicates the cracked sample with an inclination of 13°. The red arrows in (j) pointed out the Br grains in which parallel amorphous lamellae were obviously developed. The dashed box in (i) indicates a region of higher strain than in the rest of the sample.

The uniaxial deformation experiments with a strain of 0.12±0.05/0.12±0.01 (DT16-034), 0.25±0.05/0.21±0.04 (DT16-037) were achieved with a strain rate of about 2.1±0.9 $\times 10^{-5}$ s^{-1}/2.1±0.1 $\times 10^{-5}$ s^{-1} and 3.5±0.7 $\times 10^{-5}$ s^{-1}/2.9±0.6 $\times 10^{-5}$ s^{-1}, respectively (values before and after'/' indicate post-spinel and bridgmanite in sequence) (Table 1). In both experiments, post-spinel and bridgmanite show similar strain, which indicates the comparable viscosity of post-spinel and bridgmanite samples. Fig. 2 shows the microstructure of synthesized and deformed samples. The synthesized post-spinel and bridgmanite aggregates show equigranular texture with an almost homogeneous distribution of periclase in a framework of bridgmanite grains in the post-spinel sample (Fig. 2a and b). The average grain size for bridgmanite is about 10 μm, and that of periclase is about 5 μm. For the deformed samples, a crack was found in both recovered samples which developed by the relative advance of differential rams during decompression (Fig. 2c and g). The bridgmanite grains after deformation appear with ubiquitous amorphous lamellae (Fig. 2d, f, h and j), observed in bridgmanite both in single-phase and post-spinel phase samples. We consider the amorphous lamellae were formed during the treatment of sample, e.g., polishing and mounting. In our samples, we observed a larger population of amorphous lamellae in DT16-037 than DT16-034. Particularly in the post-spinel sample of DT16-037, parallel amorphous lamellae were observed in bridgmanite grains (Fig. 2j). We tend to relate the high intensity of amorphous lamellae with intense localization of dislocation, which was reported by Nzogang et al. (2018), who observed a direct correlation of amorphous lamellae with dislocation localization in the post-spinel sample deformed in Girard et al. (2016) with scanning precession electron diffraction.

The microstructure of post-spinel recovered from two deformation experiments shows different geometries of periclase. Post-spinel deformed to a low strain with a lower strain rate (DT16-034) shows equant shape of periclase (Fig. 2e and f). On the other hand, in the deformation experiment with a higher strain and strain rate (DT16-037), periclase grains show substantial strain with preferred horizontally elongated shape, although obvious interconnection was not observed (Fig. 2i and j). This is apparent in the image analysis for the pericalse distribution of DT16-037 and DT16-034 compared to the undeformed post-spinel sample (Fig. 3). Compared with the starting material (Fig. 3a, d and g), periclase in DT16-037 shows an apparent grain-size reduction, i.e., the log-normal grain population distribution is centered at smaller grain sizes, with a preferred elongated shape perpendicular to the uniaxial compression direction (Fig. 3b, f and i). By contrast, periclase grains in DT16-034 show neither visible shape preferred orientaion nor grain size reduction (Fig. 3b, e and h).

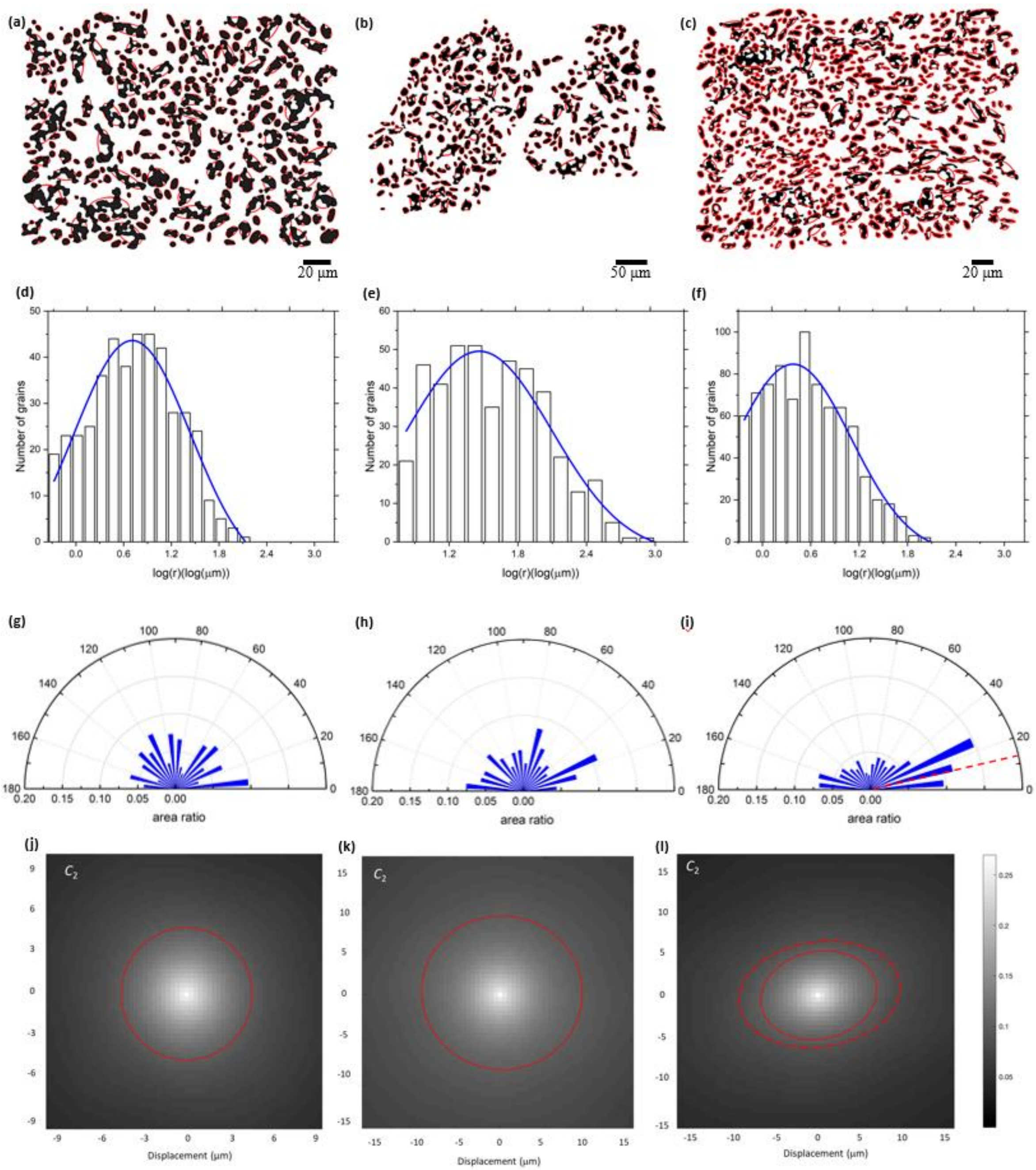

Fig.3 Image analysis for periclase distribution of undeformed sample (after synthesis) (a, d, g, j) and recovered sample with compression deformation of DT16-034(b, e, h, k) and DT16-037(c, f, i, l). The image (a) and (b) are modified from Fig.2a, e and i, respectively, to a binary image (white: bridgmanite, black: periclase). Each grain of periclase is assumed to be an ellipsoid, and the best-fit ellipsoid was calculated for each grain (shown by red

ellipsoids) for figures d-i. d-f show grain size distribution reported as a histogram of the logarithmic of the grain radius versus numbers of grains. The normal distribution curves are fit for each grain size distribution (blue lines). g-i show the periclase area-weighted orientation defined by the long axis of the ellipsoids, which is plotted as a percentage of the total periclase area. The red dashed line in (i) indicates the inclination of the sample13°due to cracking, as indicated in Fig.2g. Figures j-l show the central regions of the 2-point cluster (C_2) functions of periclase. The maximum (at zero displacement) corresponds to the volume fraction of periclase and the function decays to zero beyond the size of individual clusters. The correlation length scale, where C_2 decays to $1/e$ of its maximum value, is a good estimator of cluster size and is depicted in red. The dashed line in (l) is the correlation length scale for the high-strain region in this sample (dashed box region in Fig.2i).

Also shown in the C_2 function of (Fig. 3j-l), the circular shape of the 2-point cluster function of the undeformed sample and DT16-034 indicates the isotropic nature of periclase grains, whereas the anisotropic structure of DT16-037 is reflected by the ellipsoidal shape of the 2-point cluster correlation function. The C_2 function for an interconnected network does not decay to zero in the direction of interconnectivity; while C_2 for experiment DT16-037 is elliptical, it decays to zero within 30 μm in the stretching direction, confirming that periclase is not interconnected in this sample.

The size of clusters is well represented by the correlation lengthscale (the distance overwhich the intensity of C_2 decays to $1/e$ of its maximum value) (Heilbronner, 1992). This is presented on each image as the red ellipse. The reduction of grain size in DT16-037 is reflected by the smaller diameter of $1/e$-isoline (Fig. 3l). There is no direct evidence to prove or disprove the occurrance of dynamic recrystallization in periclase, another candidate for the grain reduction is the elongation leading to fragmentation of the grains which was proposed by Nzogang et al. (2018) for the deformed post-spinel sample of Girard et al. (2016).

The ellipticity of C_2 for experiment DT16-037 implies that, on average, periclase grains experienced 25% shortening, consistent with the bulk strain in the sample. This comparable strain of periclase and bulk sample (thus bridgmanite) indicates the strain partitioning, which could result in shear localization, doesn't occur in periclase phase, bridgmanite dominates the bulk viscosity of post-spinel sample. However, the strain in Fig. 2i is clearly hetergeneously distributed with periclase in the highlighted region showing much more horizontal elongation than elsewhere. The C_2 function for this more strongly deformed region is shown in supplementary Fig. S2 while correlation length scale ellipsoid is also shown in the Fig. 3l as the dashed ellipse. Compared with the average of the entire sample, the ellipticity of C_2 (i.e. strain of periclase) is 10% higher (with 35% shortening) while the overall correlation length of C_2 is 40% larger for the highly-deformed sub-section of the sample.

3.2 Texture

The LPOs of bridgmanite in starting material and deformed samples were calculated from 2D diffraction patterns (i.e., simulated LPOs) (Seto, 2012; Seto et al., 2010). The diffraction peaks of periclase are limited in numbers and appeared to be overlapped with the peaks of bridgmanite in most cases (Fig. S1a), we decided to use the EBSD to obtain the LPO of periclase for our post-spinel samples (see later for detailed results). Clear LPO of bridgmanite can be viewed from the intensity of diffraction peaks along azimuthal angle (Fig. S1b, c). Fig. S3 illustrates pole figures present simulated LPO of deformed bridgmanite (DT16-037) measured with different geometry. The pole figures rotate coherently with the rotation of sample direction relative to the X-ray beam direction (Fig. S3). It proves the reliability of the analysis method, and the simulated LPO patterns are not originated from the artifact. With the X-ray beam oriented along the uniaxial direction (Fig. S3c), the concentration of [100] direction is weaker compared with the orthogonal directions (Fig. S3a and b). This may result from the following two causes: (i) quality loss of the 2D diffraction pattern due to the diffraction of Pt strain marker, thermocouple, and remaining Al_2O_3 pistons along the sample column direction, and (ii) difficulty of the evaluation of the LPO developed along the direction of the X-ray incident as the case of the [100] axes.

The pole figures of synthesized bridgmanite and deformed post-spinel and bridgmanite samples are shown in Fig. 4. The starting material shows little concentration of crystallographic orientation, as shown in Fig. 4a. With uniaxial compression deformation, both DT16-034 and DT16-037, the (100) plane tends to concentrate on the compressional plane (Fig. 4b-e). It indicates that the dominant slip plane is (100) plane, consistent with Tsujino et al. (2016). Although deformed to different strains and in different samples, bridgmanite from post-spinel and bridgmanite samples from DT16-037 and DT16-034 experiments show a comparable concentration of [100] direction. To evaluate the fabric strength quantitatively, *M*-index was calculated from the distributions of uncorrelated misorientation angles (Table 1). In contrast to the starting material, in the deformed samples with strong fabric, the distribution of misorientation angles deviate from the random fabric curve, corresponding to an increase of *M*-index (Fig. S4). Fig. 5 plots calcultaed *M*-index of bridgmanite for starting material and deformed samples as a function of strain. The comparable value of the *M*-index indicates similar fabric intensity of the low strain and high strain samples, indicating a steady-state fabric strength was achieved within total strain of 0.12 under the current experimental condition. LPO is developed through rotation of grains by dislocation glide during deformation. We tend to attribute the inhibition of fabric development with strain to the growth of amorphous lamellae intensities in the recovered samples, where dislocation and strain was localized during deformation, in our samples. This is consistent with the larger population of amorphous lamellae in DT16-037 than DT16-034.

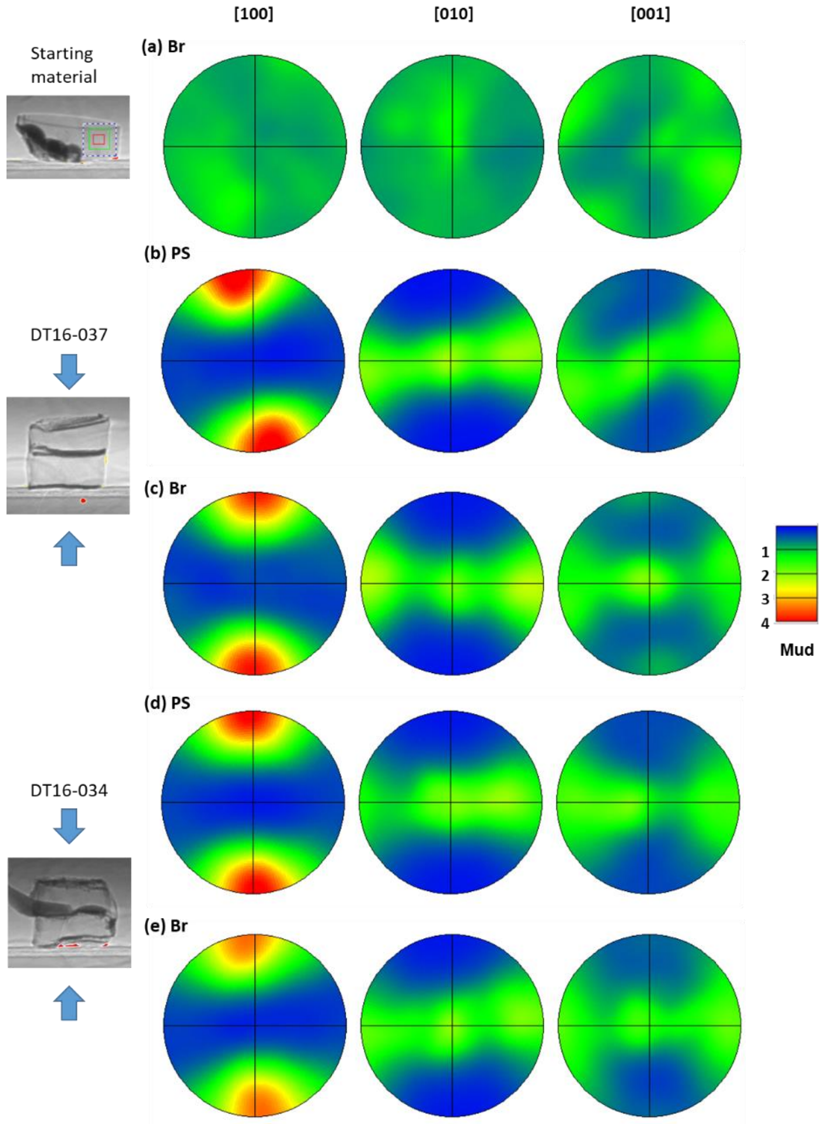

Fig. 4 Pole figures showing the simulated LPO of bridgmanite in starting material (a) and deformed post-spinel and bridgmanite samples (b-e) in the equal angle stereographic upper hemispheres projections. The sample images collected with X-ray indicate the direction of sample setting against the uniaxial compression direction (shown by arrows). The color coding refers to the density of data points, corresponds to the multiples of uniform distribution as shown in the legend. A half-width of 20° and cluster size of 10° was used for plotting and contouring.

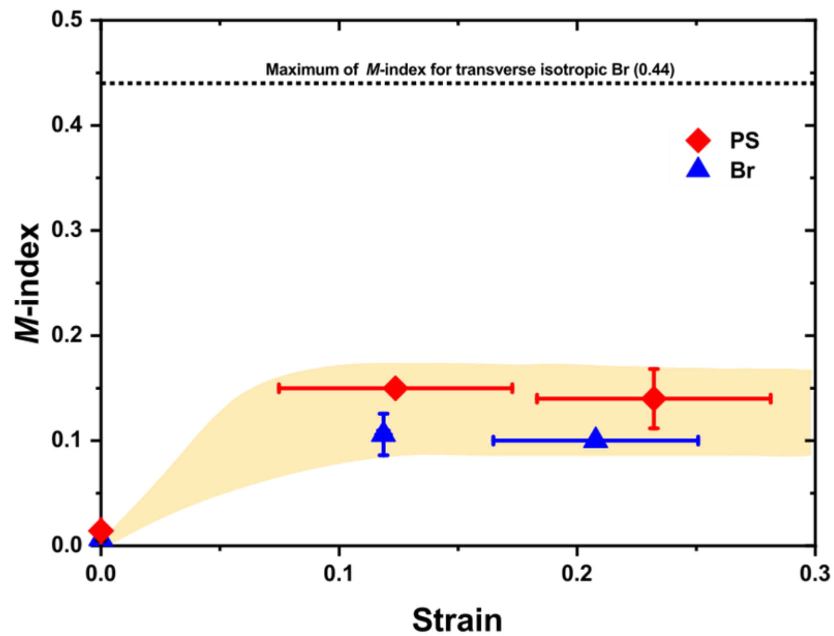

Fig. 5 Calculated *M*-index of bridgmanite for starting material and deformed post-spinel (PS) and bridgmanite (Br) samples. Error in strain derived from sample length determination by SEM image after deformation. Error in *M*-index derived from the two measurements along different directions as indicated in Fig. S3a and b. The *M*-index is 0 for random fabric and 1 for a single crystal.

Fig. 6 shows pole figures and inverse pole figures of periclase in deformed samples. In DT16-034, no noticeable fabric was observed. In contrast, a concentration of <100> axes along the compressional direction was identified in DT16-037. Also shown in the inverse pole figure, the compression direction concentrates on the <100> axes. The clear but weaker pattern of <110> and <111> axes are consistent well with the cubic crystal symmetry of periclase. The results suggest a dominant slip plane of {100} in periclase at conditions corresponding to the top of the lower mantle. Both pressure and temperature were reported to have an important but competing effect on the activities of dominant slip systems in periclase (Girard et al., 2012; Lin et al., 2019). {100} slip plane was reported by Yamazaki and Karato (2002) through deformation experiments at 0.3 GPa and 1073-1473 K. We didn't observe the second dominant slip system, i.e., {110}, they reported at 0.3 GPa, this is consistent with the prediction of less hardening of <100> than 〈110> direction with pressure by deformation on periclase single crystals at 4-9 GPa (Girard et al., 2012).

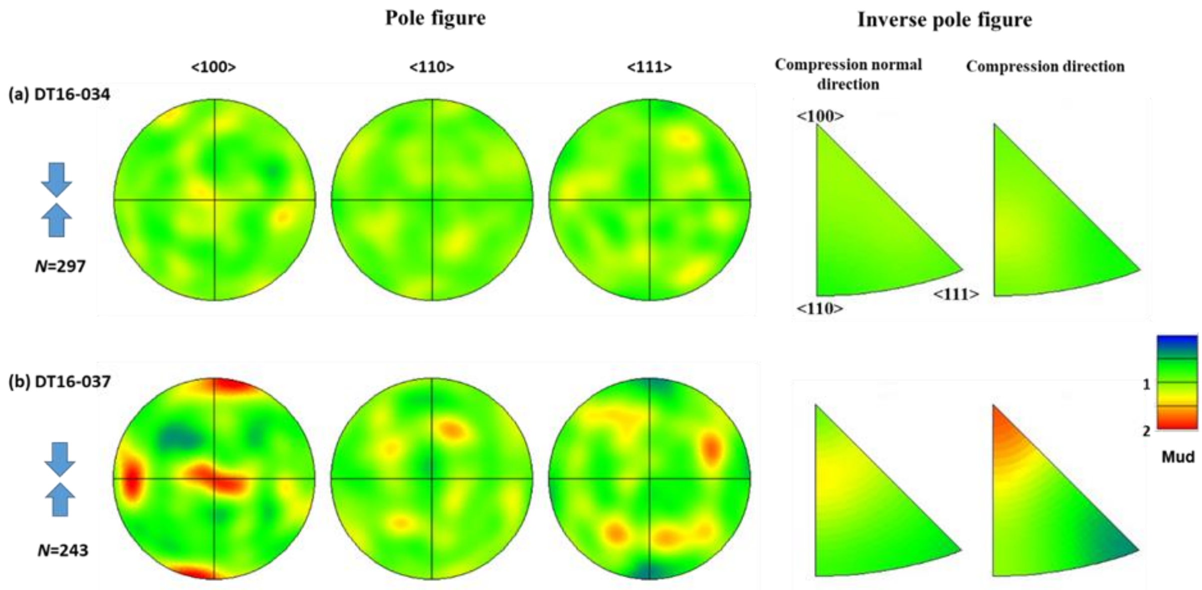

Fig. 6 Pole figure and inverse pole figure plots for the <100>, <110> and <111> orientations for periclase in deformed post-spinel samples in the equal area upper hemispheres projections obtained by EBSD measurement. The compressional deformation direction is shown by arrows. The *N* represents the number of analyzed grains. Please refer to Fig. 4 for plotting and color coding details.

4. Discussion

4.1 Comparison with previous studies

Overall, the macroscopically identical strain of bridgmanite and post-spinel samples and comparable strain of periclase grains with the bulk post-spinel sample indicate the bulk rheological property is controlled by bridgmanite in post-spinel samples without strain localization in periclase up to the strain of 0.25 ± 0.05. On the other hand, Girard et al. (2016) reported a marked softening of post-spinel aggregate with shear strain up to ~1.0, resulted in ferropericlase controlled bulk viscosity. The discordance between this study and Girard et al. (2016) highlights the significance of strain and strain rate in the bulk viscosity. Moreover, the microstructure of bridgmanite and periclase is remarkably different from the observation on the deformed sample of Girard et al. (2016) reported by Nzogang et al. (2018) using scanning precession electron diffraction. The bridgmanite shows a small deformation with a dominant slip plane of (010) inferred from activated dislocations. The prominent LPO of bridgmanite observed in our study highlights a robust deformation of bridgmanite with the dominant slip plane of (100), compatible with the dominant slip system determined by

Tsujino et al. (2016). The different structure of bridgmanite in post-spinel deformed to small strain (0.25±0.05 from our study) and high strain (~1.0 in Girard et al. 2016) highly likely indicate that bridgmanite experience less deformation with increasing bulk strain due to the accommodation of substantial strain in ferropericlase. Although intense dislocation activity and storage were observed with large strain sample recovered from Girard et al. (2016), neither LPO nor dynamic recrystallization was formed in ferropericlase (Nzogang et al., 2018). This might indicate a dominance of multiple slip system in their ferropericlase instead of the domination of one slip system in our sample. The different microstructure of bridgmanite and ferropericlase in the two studies strongly indicates a high possibility that different deformation mechanisms operated in the samples of two studies due to the different strain and strain partitioning between bridgmanite and periclase. Therefore, a comparison of both studies should be made with caution before a full understanding of the transition of deformation mechanisms.

4.2 Implications for the lower mantle

The preservation of BEAMS requires localization of strain in the weak conduits of pyrolitic material (Ballmer et al., 2017). However, for the formation of weak conduits, an 'activation strain' should be considered to initialize the strain localization in conduits as a texturally-equilibrated aggregate with isolated ferropericlase is expected after the transformation from ringwoodite to post-spinel. One good candidate is the deformation introduced by slab subduction which causes local increases in both strain rate and amount of strain. In this case, a time delay should be considered for the formation of BEAMS after the starting of tectonics and strain rates must be sufficiently high for an interconnected ferropericlase texture to form. For small amounts of deformation and very low strain rates, pyrolite and bridgmanite composition are likely to have indistinguishable rheological properties and it might therefore be hard to separate the two bulk compositions by viscosity or seismic texture.

The sample composition used in this study with post-spinel is the extreme case compared with the Earth's mantle, with likely mantle compositions (pyrolite, harzburgite, chondrite) intermediate between the post-spinel and pure bridgmanite compositions studied here. This means that in the lower mantle, any strain localization would have to occur in mixtures with higher phase proportions of bridgmanite than those studied here, and hence require even higher strains than the highest strain obtained here. A logical consequence of this is that strain localization on to periclase is more likely in Mg-enriched components such as a subducted harzburgite-composition layer, is less likely in equilibrated pyrolite component and is unlikely in basaltic composition. Two further considerations need to be made. First, normal mantle compositions do not just contain bridgmanite and ferropericlase. If the calcium-silicate perovskite phase, which is the third most abundant lower-mantle mineral, is also weak it might help to promote strain localization in the lower mantle along with ferropericlase. Second, where downwelling material enters the lower mantle, the post-spinel assembly will be formed from ringwoodite grains. If ringwoodite and garnet domains are sufficiently large in the transition zone, the texture of material subducted into the lower mantle will have separate domains dominated by post-spinel and bridgmanite (e.g., Dobson & Mariani, 2014), which themselves may form networks in which strain localization might occur. This inherited large-scale texture might therefore allow strain localization in bulk compositions with smaller ferropericlase phase fractions than expected to localize based on experiments using homogeneous mixtures. In this case, the interconnection of ferropericlase grains might be formed by deformation especially at the lower temperatures of subducting slabs (Yamazaki et al., 2014). When we consider the viscosity contrast in the lower mantle, strain rates and strain are essential parameters we should include in addition to composition heterogeneity. The current study and previous report (Girard et al., 2016) represent different strain-strain rate conditions, i.e., low strain and strain rate in our study and high strain and strain rate in their study. On the other hand, the deformation in Earth is expected to occur at extremely low strain rate, but with considerable strain. A valid extrapolation of the experimental result to the mantle may require more studies to cover a broader strain-strain rate space.

Acknowledgment

We would like to thank Hitoshi Gomi, Longjian Xie, Moe Sakurai, Chengcheng Zhao, Chao Liu, Wei Sun, Hongzhan Fei, Baohua Zhang for their help with the *in situ* experiments at BL04B1, SPring-8, Japan. We also thank Longjian Xie for helping with Python coding and Longli Guan for periclase pole figure plotting. This project has received funding from the Natural Environment Research Council (NERC) (Grant agreements NE/K002902/1 and NE/L006898/1 to DPD, and NE/P017525/2 to SAH). We thank Eiji Ito for his help with glass making at BL04B2, SPring-8. We thank Yu Nishihara, Tomoaki Kubo and Takashi Yoshino for their support on experiment at University College London. The *in situ* experiments were performed under SPring-8 Budding Researchers Support Proposals Numbers 2014B1778, 2015B1761 and 2016A1629. Visit University College London (UCL) were made available through JSPS Kakenhi #15K21712. Datasets for this research (main paper and Supporting Information) will be available at https://doi.org/10.5281/zenodo.5647996 (doi: 10.5281/zenodo.5647996).

Reference

Ballmer, M. D., Schmerr, N. C., Nakagawa, T., & Ritsema, J. (2015). Compositional mantle layering revealed by slab stagnation at ~1000-km depth. *Science Advances*, *1*(11), 1–10. https://doi.org/10.1126/sciadv.1500815

Ballmer, M. D., Houser, C., Hernlund, J. W., Wentzcovitch, R. M., & Hirose, K. (2017). Persistence of strong silica-enriched domains in the Earth's lower mantle. *Nature Geoscience*, *10*(3), 236–240. https://doi.org/10.1038/ngeo2898

Dobson, D. P., & Mariani, E. (2014). The kinetics of the reaction of majorite plus ferropericlase to ringwoodite: Implications for mantle upwellings crossing the 660 km discontinuity. *Earth and Planetary Science Letters*, *408*, 110–118. https://doi.org/10.1016/j.epsl.2014.10.009

Fukao, Y., & Obayashi, M. (2013). Subducted slabs stagnant above, penetrating through, and trapped below the 660 km discontinuity. *Journal of Geophysical Research: Solid Earth*, *118*(11), 5920–5938. https://doi.org/10.1002/2013JB010466

Girard, J., Chen, J., & Raterron, P. (2012). Deformation of periclase single crystals at high pressure and temperature: Quantification of the effect of pressure on slip-system activities. *Journal of Applied Physics*, *111*(11). https://doi.org/10.1063/1.4726200

Girard, J., Amulele, G., Farla, R., Mohiuddin, A., & Karato, S. I. (2016). Shear deformation of bridgmanite and magnesiowüstite aggregates at lower mantle conditions. *Science*, *351*(6269), 144–147. https://doi.org/10.1126/science.aad3113

Handy, M. R. (1994). Flow laws for rocks containing two non-linear viscous phases: a phenomenological approach. *Journal of Structural Geology*, *16*(3), 287–301.

Heilbronner, R. P. (1992). The autocorrelation function: an image processing tool for fabric analysis. *Tectonophysics*, *212*(3–4), 351–370. https://doi.org/10.1016/0040-1951(92)90300-U

Hunt, S. A., & Dobson, D. P. (2017). Note: Modified anvil design for improved reliability in DT-Cup experiments. *Review of Scientific Instruments*, *88*(12). https://doi.org/10.1063/1.5005885

Hunt, S. A., Weidner, D. J., McCormack, R. J., Whitaker, M. L., Bailey, E., Li, L., et al. (2014). Deformation T-Cup: A new multi-anvil apparatus for controlled strain-rate deformation experiments at pressures above 18 GPa. *Review of Scientific Instruments*, *85*(8). https://doi.org/10.1063/1.4891338

Hunt, S. A., Whitaker, M. L., Bailey, E., Mariani, E., Stan, C. V., & Dobson, D. P. (2019). An experimental investigation of the relative strength of the silica polymorphs quartz, coesite, and stishovite. *Geochemistry, Geophysics, Geosystems*, *20*(4), 1975–1989. https://doi.org/10.1029/2018GC007842

Irifune, T. (1994). Absence of an aluminous phase in the upper part of the Earth's lower mantle. *Nature*. https://doi.org/10.1038/370131a0

Irifune, T., & Ringwood, A. E. (1987). Phase transformations in a harzburgite composition to 26 GPa: implications for dynamical behaviour of the subducting slab. *Earth and Planetary Science Letters*, *86*(2–4), 365–376. https://doi.org/10.1016/0012-821X(87)90233-0

Irifune, T., Shinmei, T., McCammon, C. A., Miyajima, N., Rubie, D. C., & Frost, D. J.

(2010). Iron partitioning and density changes of pyrolite in Earth's lower mantle. *Science*, *327*(5962), 193–195. https://doi.org/10.1126/science.1181443

Kaercher, P., Miyagi, L., Kanitpanyacharoen, W., Zepeda-Alarcon, E., Wang, Y., Parkinson, D., et al. (2016). Two-phase deformation of lower mantle mineral analogs. *Earth and Planetary Science Letters*, *456*, 134–145. https://doi.org/10.1016/j.epsl.2016.09.030

Li, C., Van Der Hilst, R. D., Engdahl, E. R., & Burdick, S. (2008). A new global model for P wave speed variations in Earth's mantle. *Geochemistry, Geophysics, Geosystems*, *9*(5). https://doi.org/10.1029/2007GC001806

Li, L., Addad, A., Weidner, D., Long, H., & Chen, J. (2007). High pressure deformation in two-phase aggregates. *Tectonophysics*, *439*(1–4), 107–117. https://doi.org/10.1016/j.tecto.2007.04.004

Lin, F., Couper, S., Jugle, M., & Miyagi, L. (2019). Competing deformation mechanisms in periclase: Implications for lower mantle anisotropy. *Minerals*, *9*(11), 1–10. https://doi.org/10.3390/min9110650

Madi, K., Forest, S., Cordier, P., & Boussuge, M. (2005). Numerical study of creep in two-phase aggregates with a large rheology contrast: Implications for the lower mantle. *Earth and Planetary Science Letters*, *237*(1–2), 223–238. https://doi.org/10.1016/j.epsl.2005.06.027

Mundl, A., Touboul, M., Jackson, M. G., Day, J. M. D., Kurz, M. D., Lekic, V., et al. (2017). Tungsten-182 heterogeneity in modern ocean island basalts. *Science*, *356*(6333), 66–69. https://doi.org/10.1126/science.aal4179

Murakami, M., Ohishi, Y., Hirao, N., & Hirose, K. (2012). A perovskitic lower mantle inferred from high-pressure, high-temperature sound velocity data. *Nature*, *485*(7396), 90–94. https://doi.org/10.1038/nature11004

Nishiyama, N., Seike, S., Hamaguchi, T., Irifune, T., Matsushita, M., Takahashi, M., et al. (2012). Synthesis of nanocrystalline bulk SiO 2 stishovite with very high toughness. *Scripta Materialia*, *67*(12), 955–958. https://doi.org/10.1016/j.scriptamat.2012.08.028

Nzogang, B. C., Bouquerel, J., Cordier, P., Mussi, A., Girard, J., & Karato, S. (2018). Characterization by scanning precession electron diffraction of an aggregate of bridgmanite and ferropericlase deformed at HP-HT. *Geochemistry, Geophysics, Geosystems*, *19*(3), 582–594. https://doi.org/10.1002/2017GC007244

Ohara, K., Onodera, Y., Kohara, S., Koyama, C., Masuno, A., Mizuno, A., et al. (2020). Accurate synchrotron hard X-ray diffraction measurements on high-temperature liquid oxides. *International Journal of Microgravity Science and Application*, *37*(2), 370202. https://doi.org/10.15011/jasma.37.2.370202

Rudolph, M. L., Lekić, V., & Lithgow-Bertelloni, C. (2015). Viscosity jump in Earth's mid-mantle. *Science*, *350*(6266), 1349–1352. https://doi.org/10.1126/science.aad1929

Seto, Y. (2012). Whole pattern fitting for two-dimensional diffraction patterns from polycrystalline materials. *Review of High Pressure Science and Technology*, *22*(2), 144–152.

Seto, Y., Nishio-Hamane, D., Nagai, T., & Sata, N. (2010). Development of a software suite on X-ray diffraction experiments. *Review of High Pressure Science and Technology/Koatsuryoku No Kagaku To Gijutsu*, *20*(3), 269–276.

https://doi.org/10.4131/jshpreview.20.269

Skemer, P., Katayama, I., Jiang, Z., & Karato, S. I. (2005). The misorientation index: Development of a new method for calculating the strength of lattice-preferred orientation. *Tectonophysics*, *411*(1–4), 157–167. https://doi.org/10.1016/j.tecto.2005.08.023

Thielmann, M., Golabek, G. J., & Marquardt, H. (2020). Ferropericlase control of lower mantle rheology: Impact of phase morphology. *Geochemistry, Geophysics, Geosystems*, *21*(2). https://doi.org/10.1029/2019GC008688

Tsujino, N., Nishihara, Y., Yamazaki, D., Seto, Y., Higo, Y., & Takahashi, E. (2016). Mantle dynamics inferred from the crystallographic preferred orientation of bridgmanite. *Nature*, *539*(7627), 81–84. https://doi.org/10.1038/nature19777

Wang, Y., Hilairet, N., Nishiyama, N., Yahata, N., Tsuchiya, T., Morard, G., & Fiquet, G. (2013). High-pressure, high-temperature deformation of CaGeO3 (perovskite)±MgO aggregates: Implications for multiphase rheology of the lower mantle. *Geochemistry, Geophysics, Geosystems*, *14*(9), 3389–3408. https://doi.org/10.1002/ggge.20200

Yamazaki, D., & Karato, S. (2001). Some mineral physics constraints on the rheology and geothermal structure of Earth’ s lower mantle. *American Mineralogist*, *86*, 385–391. https://doi.org/10.2138/am-2001-0401

Yamazaki, D., & Karato, S. I. (2002). Fabric development in (Mg,Fe)O during large strain, shear deformation: Implications for seismic anisotropy in Earth’s lower mantle. *Physics of the Earth and Planetary Interiors*, *131*(3–4), 251–267. https://doi.org/10.1016/S0031-9201(02)00037-7

Yamazaki, D., Yoshino, T., & Nakakuki, T. (2014). Interconnection of ferro-periclase controls subducted slab morphology at the top of the lower mantle. *Earth and Planetary Science Letters*, *403*, 352–357. https://doi.org/10.1016/j.epsl.2014.07.017

Table

Table 1 Conditions and results of the deformation experiments.

Run No.	Pressure (GPa) [a]	Temperature (K)	Strain (%)		strain rate (10^{-5} s^{-1})		*M*-index of Br	
			PS	Br	PS	Br	PS	Br
DT16-034	~25	1773	12(5)	12(1)	2.1(9)	3.5(7)	0.15(0)	0.11(2)
DT16-037			25(5)	21(4)	2.1(1)	2.9(6)	0.14(3)	0.10(0)

Note. Number in parenthesis represents the uncertainties in the last digit. Abbreviations: PS = post-spinel; Br = bridgmanite.

[a]: The pressure of DT-Cup runs was estimated by akimotoite-bridgmanite phase transition.